

## Table of Contents

Table of Contents .....	S1
Experimental Procedures .....	S1
Characterization methods.....	S1
Results and Discussion .....	S3
Optical microscopy.....	S3
Infrared spectroscopy (FTIR).....	S4
X-ray Photoelectron Spectroscopy (XPS).....	S5
Scanning Electron Microscopy (SEM) .....	S6
Atomic Force Microscopy (AFM).....	S7
Elemental analysis.....	S8
Tunneling AFM.....	S9
Comparison of electronic properties of 2D materials.....	S10
Electron Paramagnetic Resonance spectroscopy (EPR).....	S11
Spectrophotometric determination of optical parameters.....	S12
Transient optical spectroscopy.....	S14
Simulation of nearest-neighbor transitions in three different polytypes of TGCN.....	S18
References .....	S21
Author Contributions.....	S21

## Experimental Procedures

**Synthesis of TGCN.** Adopting the method in the prior study,<sup>[1]</sup> TGCN was prepared *via* ionothermal polycondensation on a quartz glass (SiO<sub>x</sub>) substrate (5×5×1 mm) in a closed ampoule system (Scheme 1). In a typical experiment, dicyandiamide (0.5 g, 5.95 mmol) and the eutectic salt mixture of LiBr/KBr (15 g, 52:48 wt%, dried at 200 °C under vacuum overnight) were ground under inert atmosphere. A quartz glass slide was first inserted in a quartz glass ampoule (l: 120 mm, i.d.: 27 mm) and positioned parallel to the bottom surface. The powder mixture was then transferred to the ampoule and immerse the slide entirely. The loaded ampoule was vacuumed at RT, and sealed at the neck position to make a closed reaction system. The polycondensation reaction was carried out in a furnace with the heating conditions as follows: (1) ramped at 40 °C min<sup>-1</sup> to 400 °C; (2) held at 400 °C for 4 h; (3) further ramped at 40 °C min<sup>-1</sup> to 600 °C; and (4) held at 600 °C for 60 h. The SiO<sub>x</sub> slides covered with TGCN (TGCN@SiO<sub>x</sub>) were recovered from the ampoule, soaked in distilled water overnight, and rinsed thoroughly to remove residual eutectic salts from the sample. For electrical and optical experiments, the film on one face of the samples was scraped off with soft tissue, followed by cleaning the respective surface with isopropanol.

## Characterization methods

**Electrical measurements.** I-V measurements were carried out to obtain electrical conductivity for in-plane and out-of-plane of the film samples as well as bulk conductivity of the powder sample. In-plane conductivity was measured with four-point-probe method using a in-house station which consists of four independent micromanipulators (miBot™; Imina Technologies) with Tungsten needle probes, a microscope (Optem FUSION Lens System; Qioptig), and a source measure unit (4200A SCS parameter analyzer; Keithley). For four-probe methods, a thin-film assumption was applied<sup>[2]</sup> based on the following equation:

$$\sigma_{\text{in-p}} = \frac{\ln(2) I}{\pi t U}$$

The spacing (s) between each probe is approx. 66.7 μm, substantially greater than the film thickness (t) of ~306 nm (s >> t), satisfying the criteria for the thin-film assumption. Areas of ~200 × 200 μm were selected to accommodate probes (Figure S2) for in-plane measurements with four-probe method. Out-of-plane conductivity measurements were performed by a two-probe method. First, a silver (Ag) top-electrode was thermally deposited with a thickness of 100 nm onto a free-standing TGCN flake sample. The sample was then

## SUPPORTING INFORMATION

placed onto conductive gold (Au) on mica for the conductivity measurement. A current-carrying probe and a voltage-sensing probe were placed onto the Ag top-electrode above the TGCN, and the other two probes were set onto the bottom Au/mica surface. The area of Ag top-electrode ( $0.15 \text{ mm}^2$ ) was used to calculate the conductivity from the measured resistance.

Powder bulk conductivity was also measured using a stainless-steel press kit (Figure S1). TGCN powder recovered from scratching the surface of TGCN@SiO<sub>x</sub> was thoroughly ground in a mortar. The sample was then pressed in an insulating plastic insert with an inner diameter of 8 mm by two stainless rods. Current-voltage relationship was obtained from two-probe method using a source meter (Keithley 2612 A) under pressure (50 bar) at RT. Based on the sectional area of the pellet and measured thickness, we estimated the conductivity. In all three methods, at least three different samples and/or locations were measured and the averaged values are reported.

**Scanning electron microscope (SEM)** images were collected with a Nova NanoSEM 450 from FEI. TGCN@SiO<sub>x</sub> sample was directly mounted onto a 15 mm aluminum stub using a carbon tape adhesive. Imaging was conducted at a working distance of 1-8 mm and a working voltage of 10 kV using a mix of upper and lower secondary electron detectors.

**Atomic Force Microscopy (AFM)** images were obtained with Bruker Multimode VIII equipped with E-Scanner. For determining the step height, PeakForce Tapping mode with the cantilever SCANASYST-AIR was used.

**Fourier transform infrared (FT-IR)** spectra were collected at RT with Thermo Scientific Nicolet iS5 FTIR Spectrometer system in attenuated total reflection (ATR) setup.

**X-ray photoelectron spectroscopy (XPS)** was performed in an ultrahigh vacuum chamber (base pressure  $5.10 \cdot 10^{-10}$  mbar) using a JEOL JPS-9030 set-up comprising a photoelectron spectrometer hemispherical energy analyzer and a monochromatic Al K $\alpha$  ( $h\nu = 1486.6 \text{ eV}$ ) X-ray source. The XPS measurements were performed with an energy resolution of 0.9 eV as determined on a polycrystalline Ag 3d core level.



**Figure S1.** Photograph of bulk electrical conductivity measurement apparatus for powder sample.

## SUPPORTING INFORMATION

### Results and Discussion

#### Optical microscopy.

Additional height images of TGCN flakes were obtained with Olympus LEXT OLS4100 laser scanning digital microscope. While some wrinkles and cracks can be seen in some TGCN flakes, clean, flat surface for the spacing distance (200  $\mu\text{m}$ ) for I-V measurements can be identified and were selected for measurements (Figure S2).

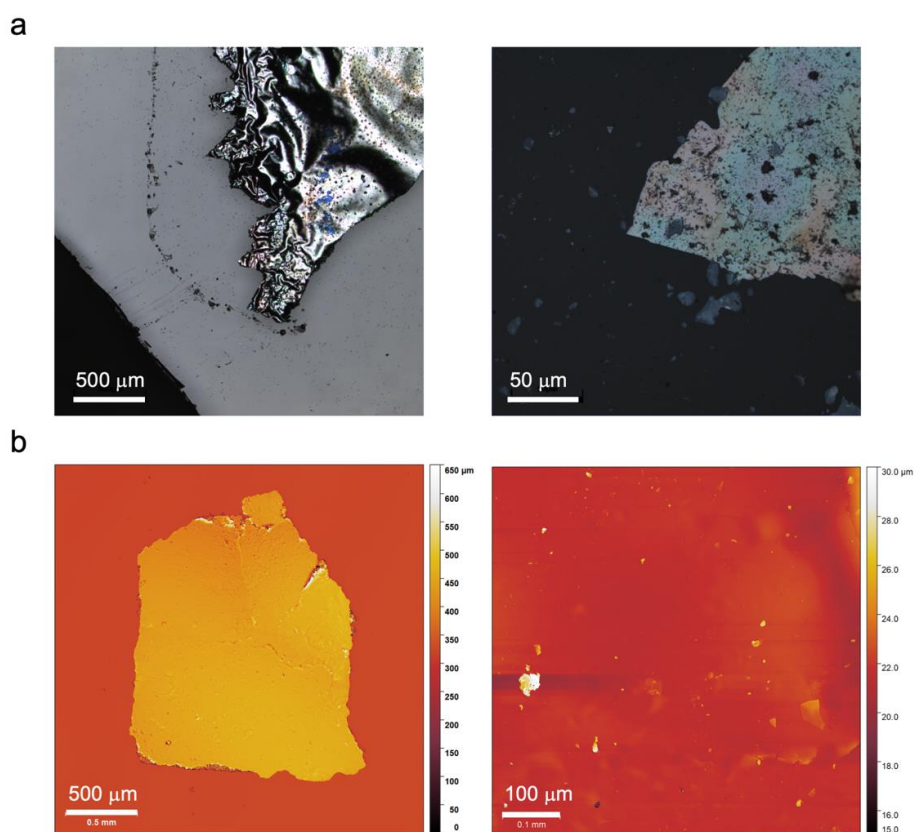


**Figure S2.** a: Optical micrographs of TGCN@SiO<sub>x</sub>. b: Height images of selected free-standing TGCN flake.

## SUPPORTING INFORMATION

### Infrared spectroscopy (FTIR).

Fourier transform infrared (FT-IR) spectra were collected at RT with Thermo Scientific Nicolet iS5 FTIR Spectrometer system in attenuated total reflection (ATR) setup. The reflective nature of TGCN surface led to features with broad bands (Figure S3). Two broad band regions from 1200-1600  $\text{cm}^{-1}$  are assigned to stretching modes of C-N and C=N in heterocycles.<sup>[3]</sup> Breathing mode of triazine units is seen at 828  $\text{cm}^{-1}$ . Finally, small presence of primary and secondary amines can also be observed, although weak and broad, from characteristic peaks 3300-3500  $\text{cm}^{-1}$ .

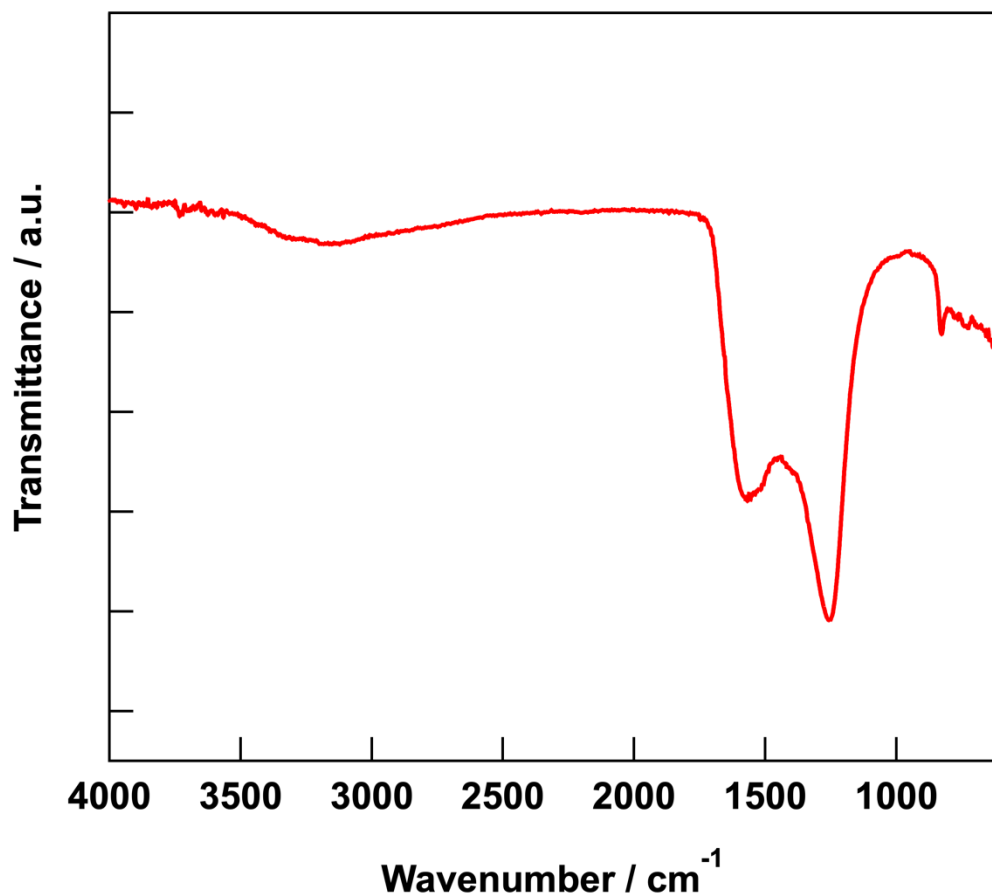
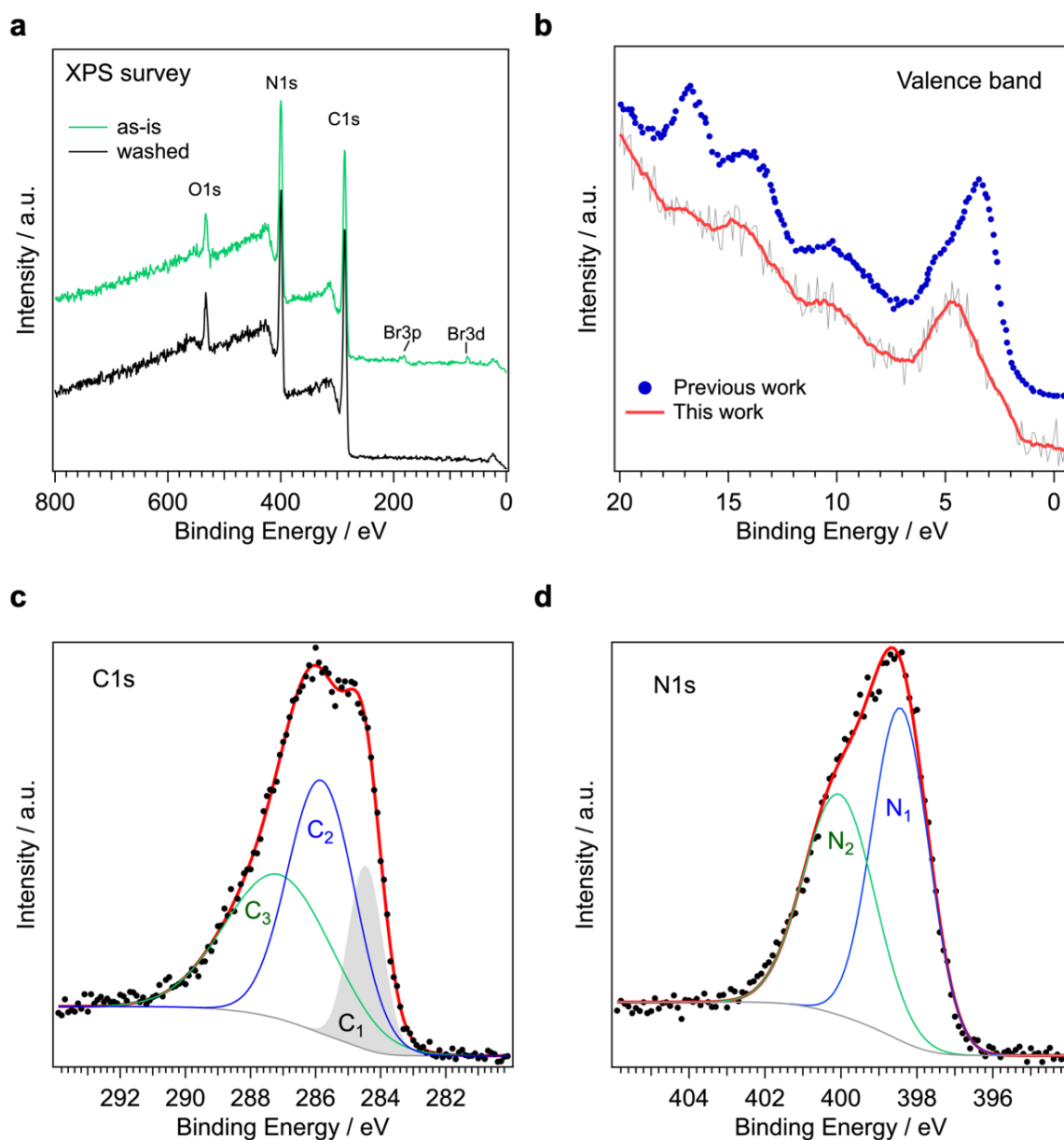


Figure S3. FTIR spectrum of TGCN film.

## SUPPORTING INFORMATION

### X-ray Photoelectron Spectroscopy (XPS).

The survey spectrum confirms some residual Br in as-is sample from the synthesis, which was well removed and cleaned with thorough rinsing with H<sub>2</sub>O (Figure S4a). The valence band structure was consistent with the previous report (Figure S4b).<sup>[1]</sup> The peak in C 1s spectrum (Figure S4c) was deconvoluted into three Gaussian components (C<sub>1-3</sub>: 284.5, 285.8, and 287.1 eV). Based on the prior reports on carbon nitride materials,<sup>[4]</sup> we assign C<sub>1</sub> (284.5 eV) to graphitic and amorphous adventitious carbon, C<sub>2</sub> (285.8 eV) to sp<sup>2</sup> carbon (trigonal configuration) bonded to nitrogen, and C<sub>3</sub> (287.1 eV) to sp<sup>3</sup> carbon (tetrahedral configuration) bonded to nitrogen. C<sub>2</sub> (44.0%) component is the highest representing the ideal triazine core unit in the structure, with some presence of surface carbon contamination and terminal and/or defect C-N bonds. The ideal, thermodynamically stable structure of TGCN should have only one type of sp<sup>2</sup> carbon configuration. However, different polymorphs of carbon nitride have been shown and they may contain sp<sup>2</sup> and sp<sup>3</sup> bonding.<sup>[5]</sup> In N 1s region (Figure S4d), two peaks were fitted to the spectrum centered at 398.4 and 400.0 eV, denoted as N<sub>1</sub> and N<sub>2</sub>, respectively. The peak at lower binding energy N<sub>1</sub> was assigned to nitrogen in the triazine ring (C-N=C, 54.8%), and the higher energy N<sub>2</sub> to nitrogen bonded to three carbon atoms.<sup>[1, 6]</sup>



**Figure S4.** XPS spectra of TGCN. **a:** Survey spectra of as-is sample and after H<sub>2</sub>O rinsing. **b:** Valence band spectrum with our previous work.<sup>[1]</sup> **c:** C1s spectrum. **d:** N1s spectrum.

## SUPPORTING INFORMATION

### Scanning Electron Microscopy (SEM)

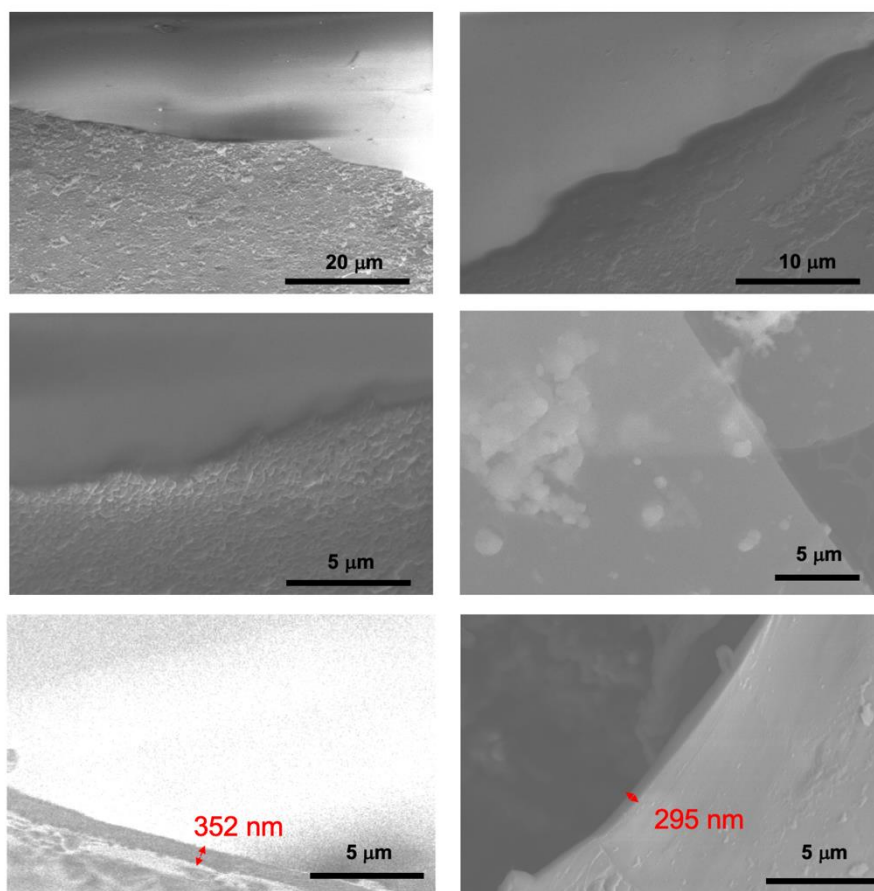
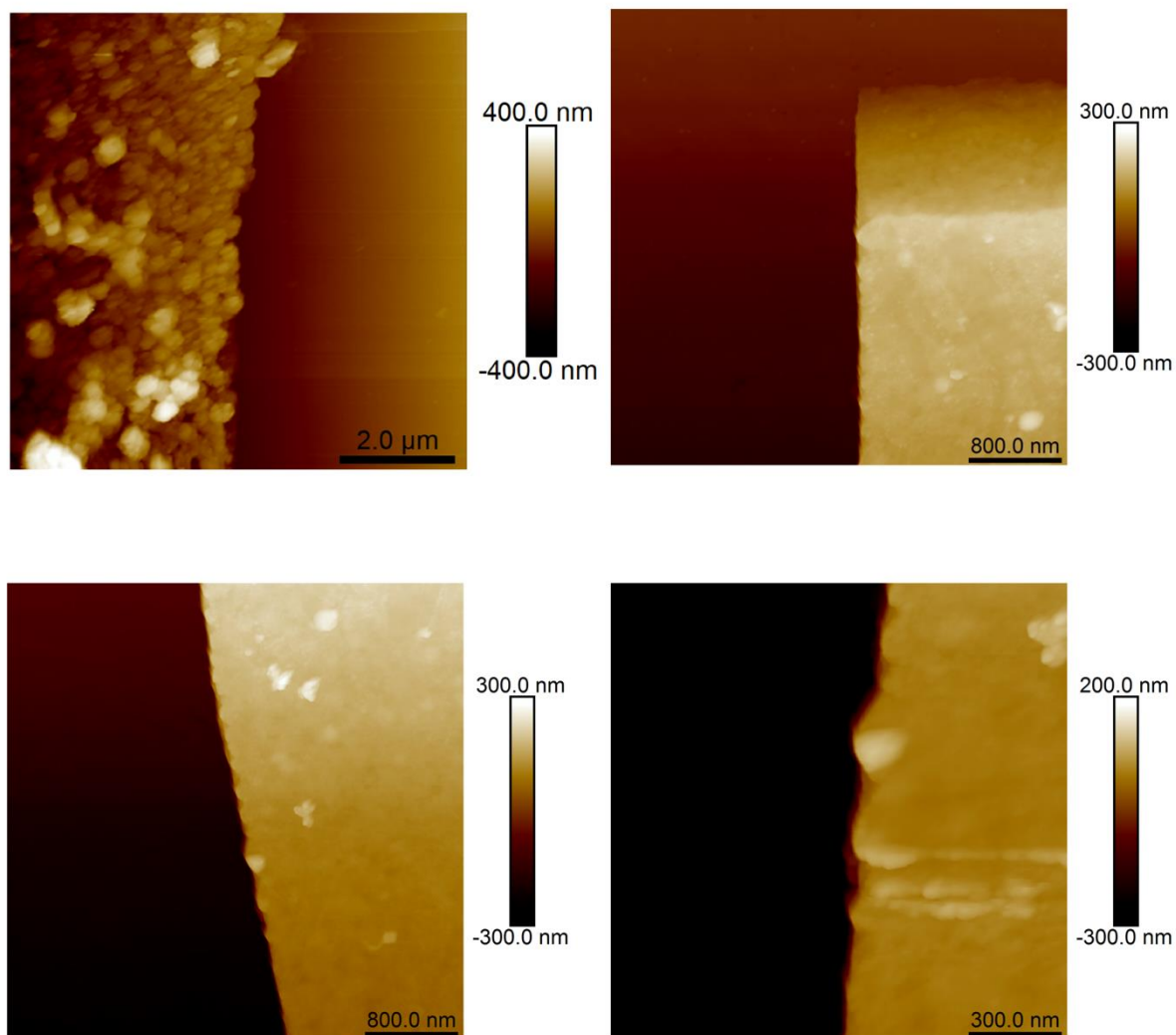


Figure 5. SEM images of TGCN@SiO<sub>x</sub>.

## SUPPORTING INFORMATION

### Atomic Force Microscopy (AFM).

Uneven rough surface can be found in most parts of as-synthesized TGCN@SiO<sub>x</sub>. Some edges still show relatively clean, flat surface, as revealed with AFM shown below (Figure S6). These areas are selected for electrical measurements. After rigorous rinse and mechanical cleaving, flatter surface can be found with higher chance.



**Figure S6.** AFM images of TGCN@SiO<sub>x</sub>.

## SUPPORTING INFORMATION

---

### Elemental analysis.

Based on the CHN elemental analysis, C/N atomic ratio was calculated as ~0.77, close to 0.75 for the ideal composition of  $C_3N_4$ . Loss of nitrogen should arise from gaseous side products such as ammonia during the synthesis.

**Table S1.** Elemental analysis of TGCN

Element	wt%
C	37.8
H	2.1
N	57.0

## SUPPORTING INFORMATION

### Tunneling AFM.

As a qualitative supporting evidence for conductive nature of TGCN film, Tunneling AFM (TUNA) was also conducted as a mode of conductive-AFM using Bruker Multimode VIII equipped with E-Scanner. Bruker SCM-PIC cantilever was used. For TUNA measurement, the TGCN film grown on  $\text{SiO}_x$  was mechanically transferred onto copper adhesive tape and mounted on a AFM sample disc. A pseudo I-V profile was obtained at a selected area based on average current recorded for each set of scans (typically  $2 \times 0.5 \mu\text{m}$ ) at different bias. A quantitative analysis is highly challenging because of the difficulty in determination of actual contact area and contact resistance, and not the scope of this study. This result however clearly confirms out-of-plane conductivity of TGCN film (Figure S7). Compared with the two-point method adopted in the study, the level of observed current of sub-pA is substantially lower, and some probable reasons are (i) great contact resistance at surface of TGCN and copper adhesive (ii) smaller contact area, and (iii) contamination at the AFM tip for additional resistance, among others. The two-probe method can be improved with a TGCN sample with both sides with deposited electrodes. However, at this time, we are unable to succeed in preparing such electrodes on the flake via deposition with precise positioning. Both TUNA and the two-probe measurements share the fundamental challenge of electrical contact and determination of its area, and this merits further research. Given the controlled Ag area size by deposition and substantially larger, stable current reading obtained from the out-of-plane measurement, we concluded that this method was much reliable and superior to TUNA in our study.

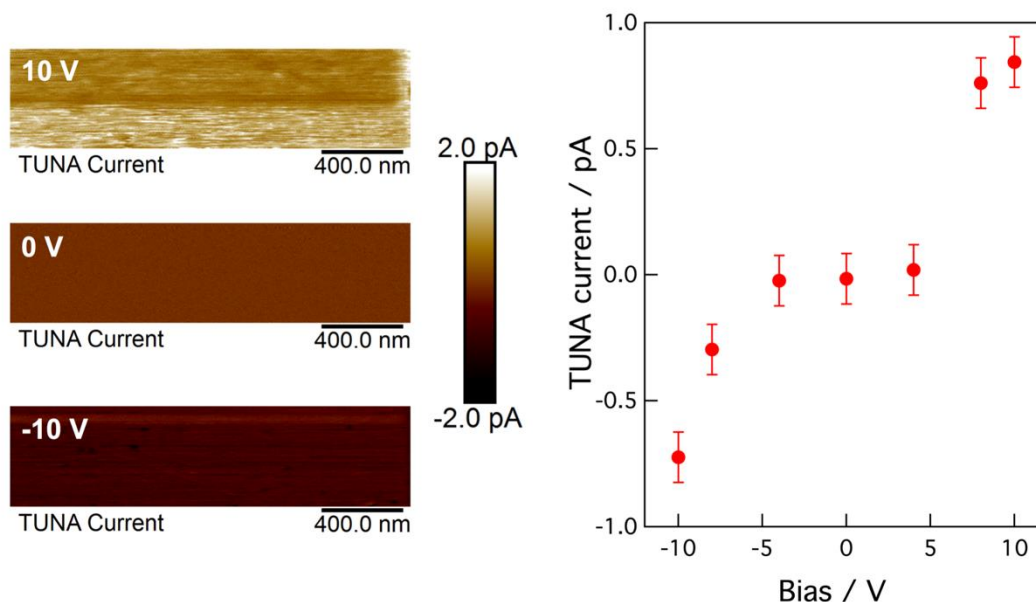


**Figure S7.** TUNA current images of TGCN at different applied bias.

## SUPPORTING INFORMATION

### Comparison of electronic properties of 2D materials.

**Table S2.** Comparison of electronic properties of 2D materials

Material	Type	Conductivity [S m <sup>-1</sup> ]	Mobility [cm <sup>2</sup> V <sup>-1</sup> s <sup>-1</sup> ]	Band gap [eV]
Graphene <sup>[7]</sup>	Conductor	10 <sup>2</sup> – 10 <sup>3</sup>	>15000	-
Hexagonal boron nitride <sup>[8]</sup>	Insulator	-	-	5 – 6
Borocarbonitride <sup>[9]</sup>	Semiconductor	~10 <sup>5</sup>	5 – 20	1.0 – 3.9
MoS <sub>2</sub> <sup>[10]</sup>	Semiconductor	~10 <sup>-2</sup>	1 – 8	1.2 – 1.9
Polyporphyrin-core COF <sup>[11]</sup>	Semiconductor	7.9 × 10 <sup>-6</sup> (out-of-plane) 2.4 × 10 <sup>-4</sup> (in-plane)	-	-
Graphdiyne nanowire <sup>[12]</sup>	Semiconductor	1.9 × 10 <sup>3</sup>	7.1 × 10 <sup>2</sup>	-
Tetrathiafulvalene-based COF <sup>[13]</sup>	Semiconductor	1.2 × 10 <sup>-4</sup> (pristine) <sup>[13a]</sup> 0.28 (I <sub>2</sub> doped) <sup>[13a]</sup> 1.8 × 10 <sup>-4</sup> (I <sub>2</sub> doped) <sup>[13b]</sup>	-	-
Melon-like polymeric carbon nitride <sup>[14]</sup>	Semiconductor	-	10 <sup>-6</sup> – 10 <sup>-4</sup>	2.7
TGCN film (this work)	Semiconductor	1.6 × 10 <sup>-6</sup> (in-plane) 1.0 × 10 <sup>-4</sup> (out-of-plane)	0.8 – 2.4	1.4 – 2.0

## SUPPORTING INFORMATION

### Electron Paramagnetic Resonance spectroscopy (EPR).

All EPR experiments were performed on an EMX<sup>plus</sup> CW (continuous wave) spectrometer (*Bruker*, Germany) equipped with the *Premium*-X-band microwave bridge. The  $g_{\text{center}}$ -factor (position corresponding to  $dI_{\text{EPR}}/dB = 0$ ) of paramagnetic centers in TGCN was determined using a built in spectrometer frequency counter and an ER-036TM NMR-Teslameter within a standard rectangular EPR cavity, ER-4102003-ST (all *Bruker*, Germany). Quantitative EPR analysis was carried out within the ER-4105000-DR double rectangular cavity using the “strong pitch” reference sample with known number radicals  $3 \cdot 10^{15}$  spins / effective cm (tube length). A second identical EPR tube was filled with the powdered sample. In order to provide the filling factor as closed as possible for both samples, their tubes were positioned within the effective EPR cavity volume by the same way. Following instrumental parameters were used for quantitative measurements: microwave frequency = 9.8124 GHz, central field = 349.95 mT, sweep width = 12 mT, receiver gain =  $1 \cdot 10^4$ , modulation frequency = 100 KHz, resolution 2001 points, power = 2.00 mW, modulation amplitude 0.06 mT, conversion time 16 ms and time constant = 10.2 ms. Several sweeps/accumulations were used in order to enhance the signal-to-noise ratio. For determination of number of paramagnetic centers in TGCN powder the double integrals of sample EPR signal and that of the reference (“strong pitch”) were compared and the number of spins was calculated from nine independent experiments as we already reported elsewhere.<sup>[15]</sup> By quantitative EPR analysis, we determined the number of paramagnetic centers in TGCN-powder:  $(1.1 \pm 0.2) \times 10^{15}$  spins per milligram of sample, which corresponds to  $(1.9 \pm 0.3)$  nmol per milligram of TGCN powder.

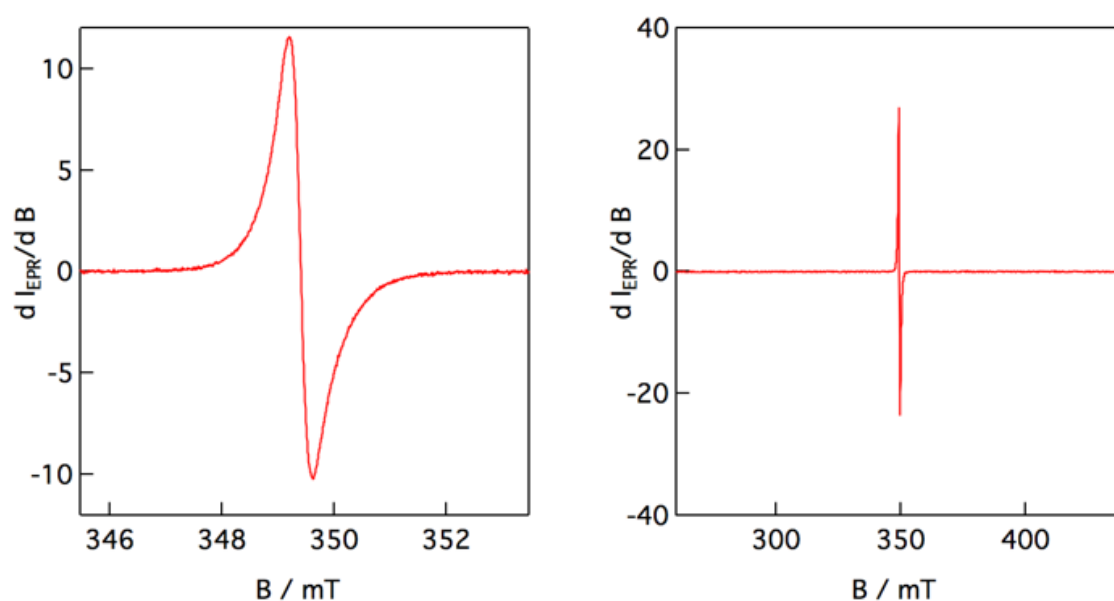


Figure S8. EPR spectra of TGCN.

## SUPPORTING INFORMATION

### Spectrophotometric determination of optical parameters.

For spectrophotometric measurements, we reverted to large specimens (> 15mm) recovered from the surface of the quartz reaction ampoule, as the samples used for the other experiments are too small for quantitative analyses. The measurements were performed with a UV-VIS-NIR spectrophotometer (Perkin-Elmer, Lambda 950), equipped with an integrating sphere to collect also the diffusely scattered light. Total transmittance (reflectance) spectra were obtained by attaching the samples to the entrance (exit) aperture of the integrating sphere, with the TGCN films oriented towards the incoming light. No explicit polarization was imposed on the probe light, and vertical incidence was used throughout these measurements.

To calculate the optical parameters of the thin TGCN films from the measured T / R spectra, a Fresnel-coefficients-based Transfer-Matrix method is used, as introduced by Harbecke.<sup>[16]</sup> Here, it is assumed that the light propagates in a strictly coherent manner within the film, while complete incoherence governs the substrate.<sup>[17]</sup> The optical parameters of the substrate were modeled using Sellmeier equations for fused silica,<sup>[18]</sup> with a thickness of 1.5 mm. The formulas for  $T(N, \lambda, d_{\text{layer}}, d_{\text{substrate}})$  and  $R(N, \lambda, d_{\text{layer}}, d_{\text{substrate}})$  were simultaneously fit to the experimental values of T and R, yielding the complex refractive index  $N = n + ik$ , and film thickness  $d_{\text{layer}}$ . Since the used formulas are oscillatory, yielding a multi-branched solution for  $N$ , a physically meaningful solution branch needs to be chosen. The absorption coefficient of the TGCN film is derived from the imaginary part  $k$  of the refractive index as  $\alpha = 4\pi k/\lambda$ . This quantity was further used to determine the energetic width of the direct and indirect optical gap by applying linear fits in the appropriate Tauc plots.<sup>[19]</sup>

The respective results are depicted in Figure S9. Panel A shows the real and imaginary part of the complex refractive index; the film thickness obtained from the fit is  $d = 84(5)\text{nm}$ . The corresponding absorption coefficient  $\alpha$  is plotted in panel C, exhibiting the steep increase in absorption for  $\lambda \leq 700\text{nm}$ . In combination with the substantial refractive index ( $n \geq 1.8$  throughout the whole visible range) this explains the dark-red color of the films, as well as the almost metallic reflectivity of the thicker flakes of TGCN. In order to gain more insight into the nature of the optical gap as compared to the earlier diffuse-reflectance study,<sup>[1]</sup> we plot the square and the square-root of the absorption coefficient vs. the photon energy in panels B and C, respectively. These Tauc plots allow to obtain the direct (indirect) optical gap energy by fitting straight lines to the slope of the respective graph (indicated in red). From the intersections with the baselines, we get  $E_{\text{G}}^{\text{dir}} = 2.026(4)\text{eV}$  and  $E_{\text{G}}^{\text{ind}} = 1.391(2)\text{eV}$ , whereby the given uncertainty is solely derived from the linear fit. These analyses do not give a definite answer as to whether the optical gap is indeed direct or indirect. However, given the over-all better fit of the direct gap, together with the steep onset and high absolute value of the absorption coefficient, we currently tend to see the result as a support of the hypothesis of a direct gap around 2 eV.<sup>[1]</sup> The other question is of course if it is appropriate to speak of a semiconductor-like band gap or a molecule-like HOMO-LUMO gap. The latter would be direct by definition, and is corroborated by observations in melon, whose optical properties seem to be largely governed by those of its constituting heptazine monomer.<sup>[20]</sup> Moreover, since the presented results have not been obtained from large planar films with homogeneous thickness, further measurements are needed to decide these questions and also provide more reliably quantitative data for the optical parameters.

## SUPPORTING INFORMATION

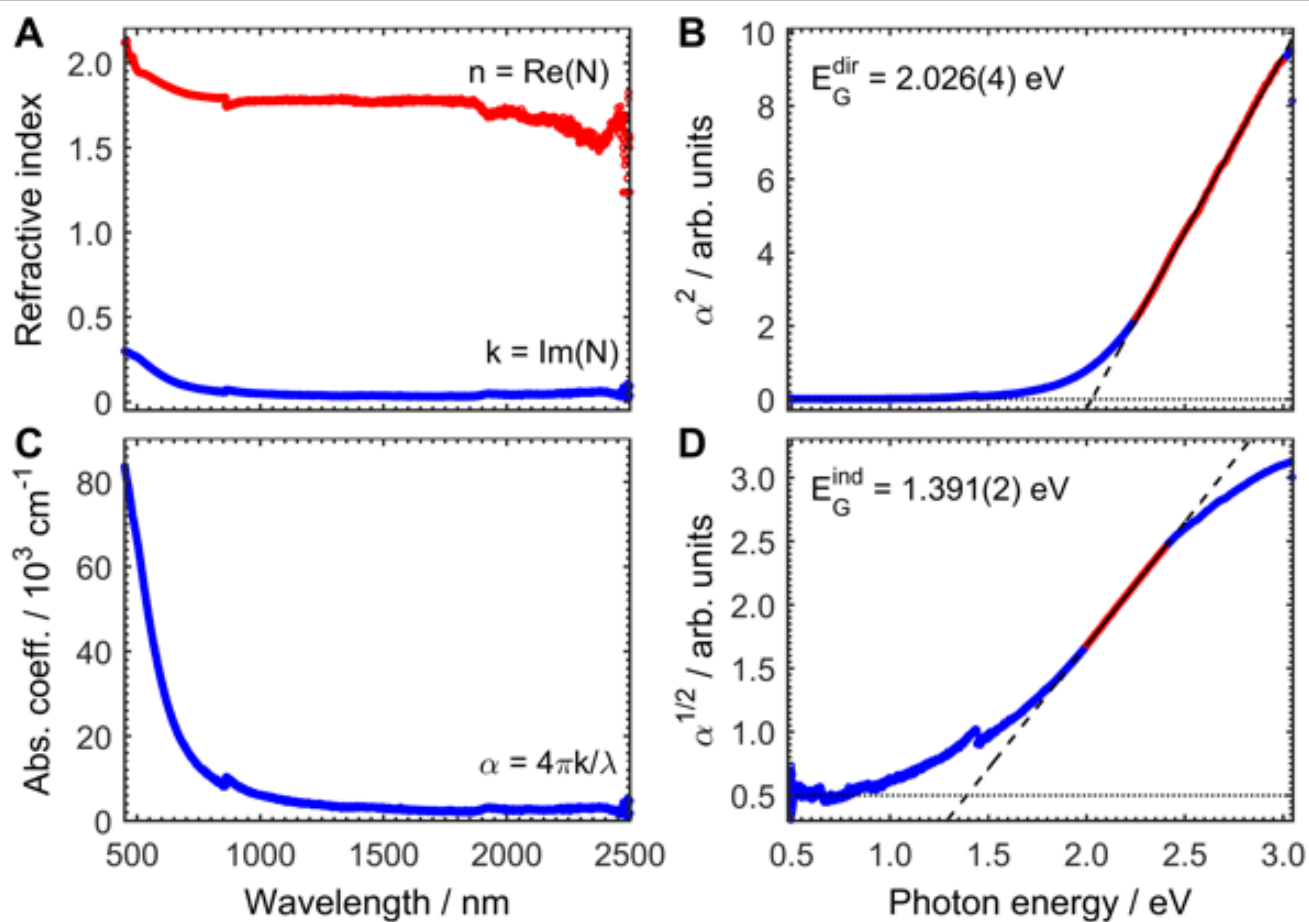


**Figure S9.** Optical parameters of TGCN films. A, C: complex refractive index and absorption coefficient  $\alpha$ . B, D: Tauc plots, showing the determination of the direct and indirect optical gap from the absorption coefficient.

## SUPPORTING INFORMATION

### Transient optical spectroscopy.

Transient photoluminescence (TRPL) spectroscopy was performed using a setup pumped by a regenerative Ti:Sapphire amplifier system (CPA-2001, Clark MXR) that generates light pulses at 775 nm with pulse durations of 150 fs at a repetition rate of 1 kHz. The excitation pulses centered at 388 nm were generated by frequency doubling with a BBO crystal and used without further compression. The time-resolved emission spectra were recorded under right-angle incidence by a streak camera system (Streakscope C10627, Hamamatsu) in a range between 350 – 950 nm. No measurable signal from TGCN flakes or films could be observed in this spectral range at ambient temperature.

Transient absorption (TA) spectroscopy was performed using a custom-built setup in standard transmission geometry with near-vertical incidence of pump and probe light. The used setup is pumped by a commercial Ti:sapphire laser system (Coherent Inc., Legend Elite Duo), delivering pulses of 25 fs duration at 800 nm central wavelength and 2.5 mJ pulse energy with a repetition rate of 5 kHz.<sup>[21]</sup> About 0.2 mJ were split off the fundamental pulses and used for generating pump light pulses. The linearly polarized excitation pulses centered at 400 nm were generated by frequency doubling with a BBO crystal and used without further compression. The maximum energy of the pump beam was about 3.2  $\mu$ J per pulse at the sample and the excitation spot had a  $1/e^2$  diameter of 500  $\mu$ m. The absorption changes were probed over the whole visible and near-infrared spectral range with a white light continuum. Here, IR pulses centered at 1300 nm, as generated by an optical-parametric amplifier (Coherent Inc. OPerA Solo) were used for supercontinuum generation in a 3 mm thick c-cut sapphire substrate. The probe pulses were not further polarized. After passing through the sample, the probe pulse was spectrally dispersed using a Czerny-Turner spectrograph (Andor Technology, Shamrock 303) and detected with multichannel detectors for the VIS and IR regions, respectively (Andor Technology, Newton & iDus). Transient spectra were recorded up to a pump-probe delay of 1.9 ns using an optical delay stage. A semi-logarithmic delay scheme was utilized, providing a dense linear sampling during the excitation period (-2 to +2 ps), and logarithmic sampling over the subsequent 3 decades.<sup>[22]</sup> The chirp of the probe light was corrected numerically during the fit procedure, i.e., in parallel with the fit of the kinetic model, by applying the formalism introduced by Kovalenko et al.<sup>[23]</sup> In this way, distortion of the original data, as is inevitable in pre-fit chirp-correction,<sup>[22]</sup> is prevented.

Fitting of the data was achieved by using the kinetic model described in the main text. The obtained population traces were shifted for each spectral bin according to the determination of time-zero by the chirp formula, convolved with the spectrally dependent Gaussian probe-pulses, and subsequently interpolated to the experimental time axis. Species-associated spectra were obtained by numerical inversion, assuming that temporal and spectral features of the involved states are mutually independent.<sup>[24]</sup>

The kinetic model described in the main text can be cast into the following rate equation system:

$$\begin{aligned} \frac{d[\text{GS}]}{dt} &= -I_p(t)[\text{GS}] + k(1 + kt)^{\alpha-1}[\text{MS}]^2 \\ \frac{d[\text{MS}]}{dt} &= \frac{-d[\text{GS}]}{dt}, \end{aligned} \quad \text{Equation S1}$$

where

$$I_p(t) = A_0 \exp \left[ \frac{-1}{2} \left( \frac{t - t_0}{\sigma_p} \right)^2 \right]$$

denotes the excitation by the pump pulse and  $k$  is a measure of the combined electron/hole hopping rates. The result of the fit procedure is depicted in Figure S10, showing the original data, the global fit results, and the residual in the left column. The right column shows the same data after chirp correction, as it is also used in the main text.

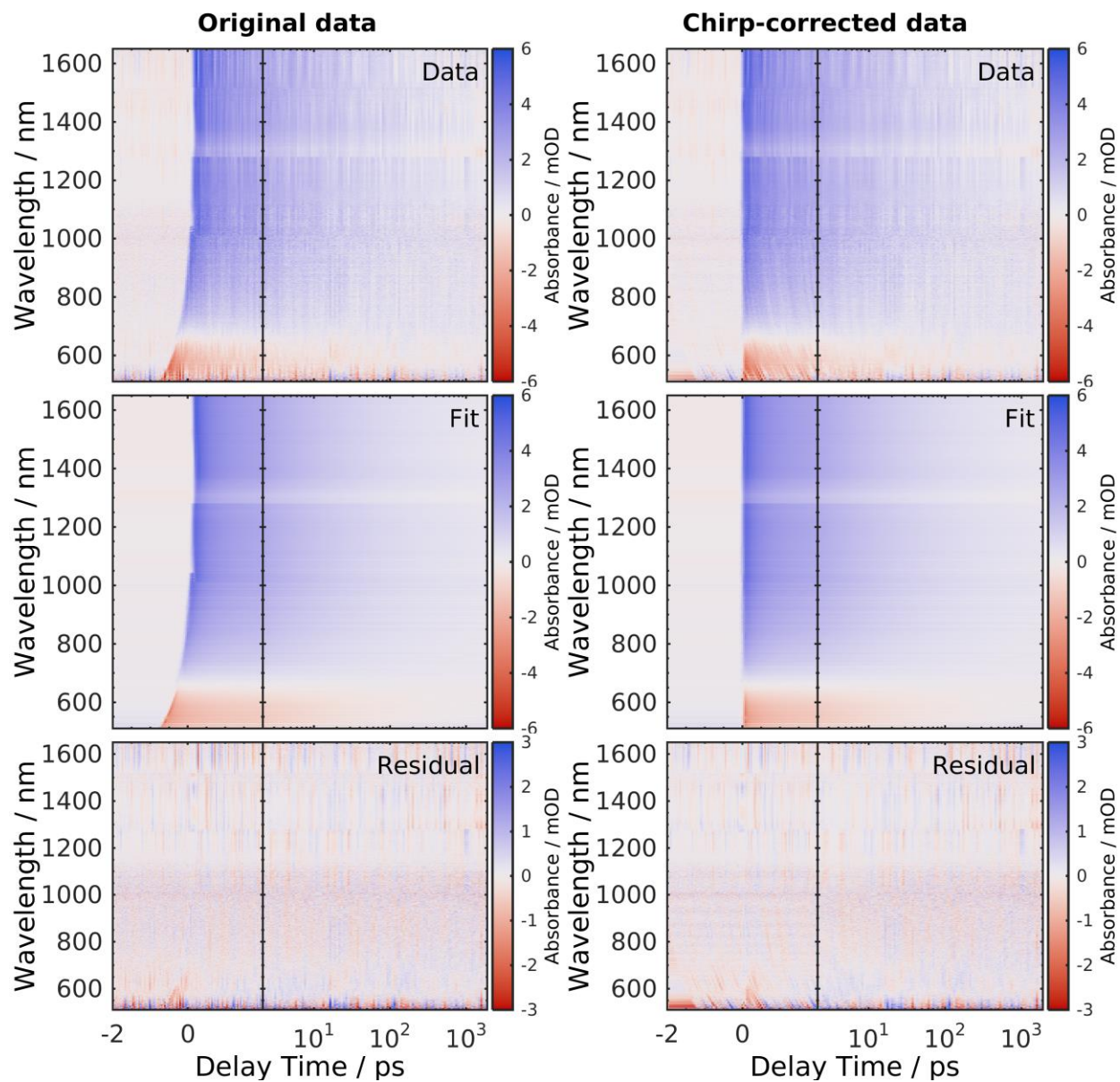


**Figure S10.** Result of the global fit procedure for the TA data recorded at 0.32  $\mu\text{J}$  pump pulse energy. Left: original data, fit, and residual. Right: same as left, but with chirp- correction applied.

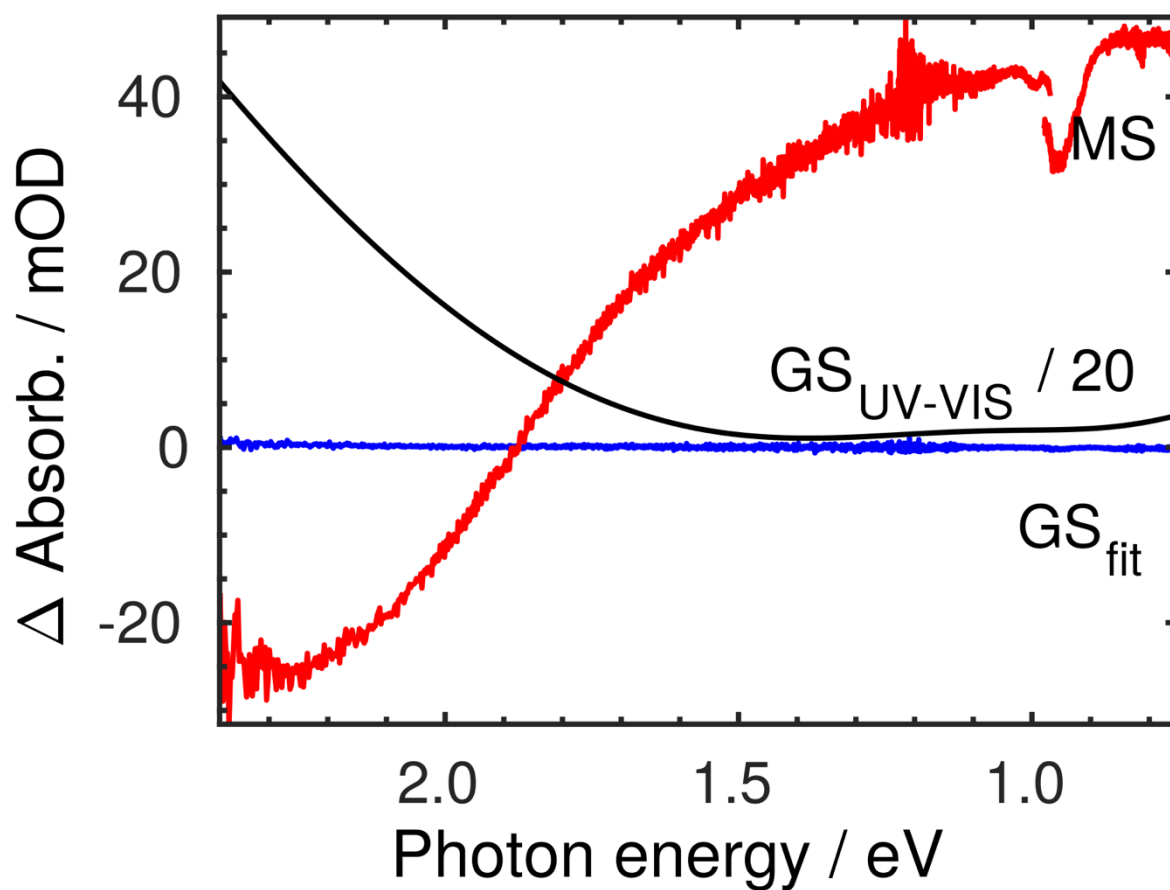


**Figure S11.** Species-associated spectra for the ground state (GS) and the metastable state (MS) for the fit shown in Figure S10; the line denoted  $GS_{UV-VIS}$  corresponds to the GS absorbance assuming the absorption coefficient of Figure S9, and a film thickness of 306 nm. Note: The dip in the transient spectra around 1 eV (see also Figure 4A in the main text) is an artifact of the strong residual 1300 nm pump light used to generate the supercontinuum.

## SUPPORTING INFORMATION

**Table S3.** Parameters obtained by the global fit routine for the TA datasets recorded at 0.32  $\mu\text{J}$  and 1.60  $\mu\text{J}$  pump pulse energy

Parameter	Value (0.32 $\mu\text{J}$ )	Value (1.60 $\mu\text{J}$ )	Unit
Pump pulse duration $\sigma_p$	45(2)	47(5)	fs
Pump rate coefficient $A_0$	1.36(3)	1.02(3)	$\text{ps}^{-1}$
Hopping rate coefficient $k$	62(4)	105(7)	$\text{ps}^{-1}$
Characteristic exponent $\alpha$	0.318(4)	0.424(4)	-

## SUPPORTING INFORMATION

---

### Simulation of nearest-neighbor transitions in three different polytypes of TGCN.

For an estimation of nearest-neighbor hopping transition probabilities, we consider three different polytypes of TGCN: the buckled AB-stacked structure (AB) and two ABC-stacked structures (ABC1, ABC2).<sup>[1]</sup> The estimation is performed by the following procedure:

- (1) Create a  $2 \times 2 \times 2$  cell of the respective structure, as well as a  $6 \times 6 \times 6$  supercell, then identify the aromatic rings in each cluster
- (2) For each ring determine the centroid and the normal vector, the latter using a least-squares fit of a 3-dimensional plane to the atom positions.
- (3) Approximate the aromatic system by the sum of 6 p-orbitals, each placed at one atom site, and oriented along the ring's normal. The  $1/e$  value of the p orbitals is defined at  $r = 0.7$  Angstrom (approximate covalent radius of C and N).
- (4) Determine the overlap integral of each ring in the  $2 \times 2 \times 2$  cell with each ring in the  $6 \times 6 \times 6$  supercell by numerical integration. The absolute square of this value is a measure of the transition probability.
- (5) Explicitly forbid or allow the in-plane nearest-neighbor transitions. In both cases, account for the highest-probability transitions down to a threshold (in this case: 1% of the most probable transition). Re-normalize the probabilities to the cumulative sum of the accounted-for probabilities.
- (6) For visualization, plot the  $2 \times 2 \times 2$  cell, together with the transitions accounted for. The strength of the transition is depicted by the thickness of the respective joint, as well as by the color code (blue-green: low probability, orange-red: high probability).

The results are shown in Figure S12.

In addition, we performed random-walk simulations of a single carrier using the structures and probabilities calculated above. For this, the number of non-equivalent rings in each polytype was determined (6 for AB, 3 for ABC1, 9 for ABC2). Each of the 1000 walks commenced at the same site, with a duration of 200 steps. The resulting traces are shown in Figure S13 for both situations: with and without allowed in-plane transitions.

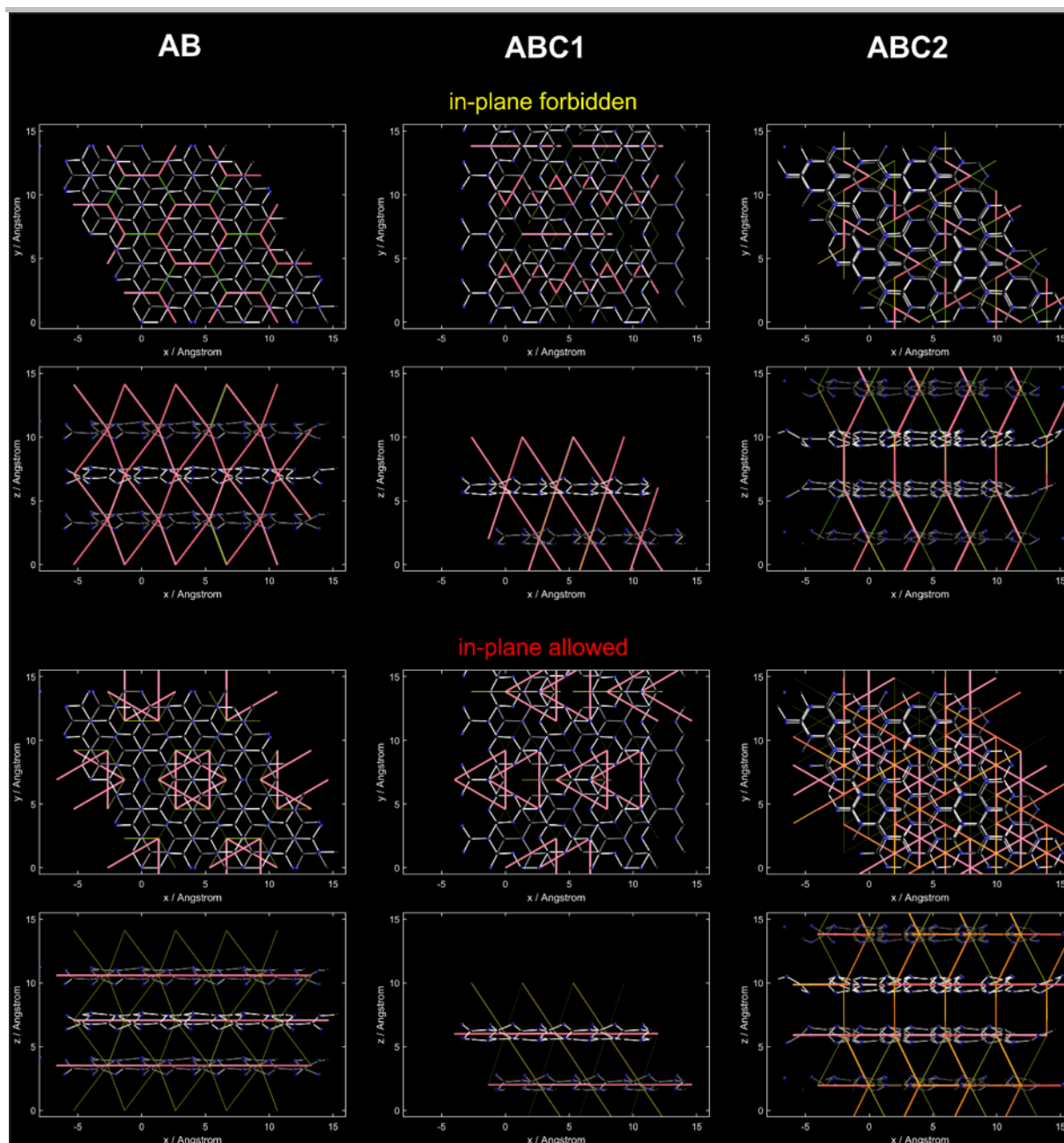


**Figure S12.** Nearest-neighbor transitions for a carrier in the three crystal polytypes of TGCN under consideration. The upper 6 panels exclude the in-plane transitions. For each case, both projections along the z and y direction are shown, respectively.

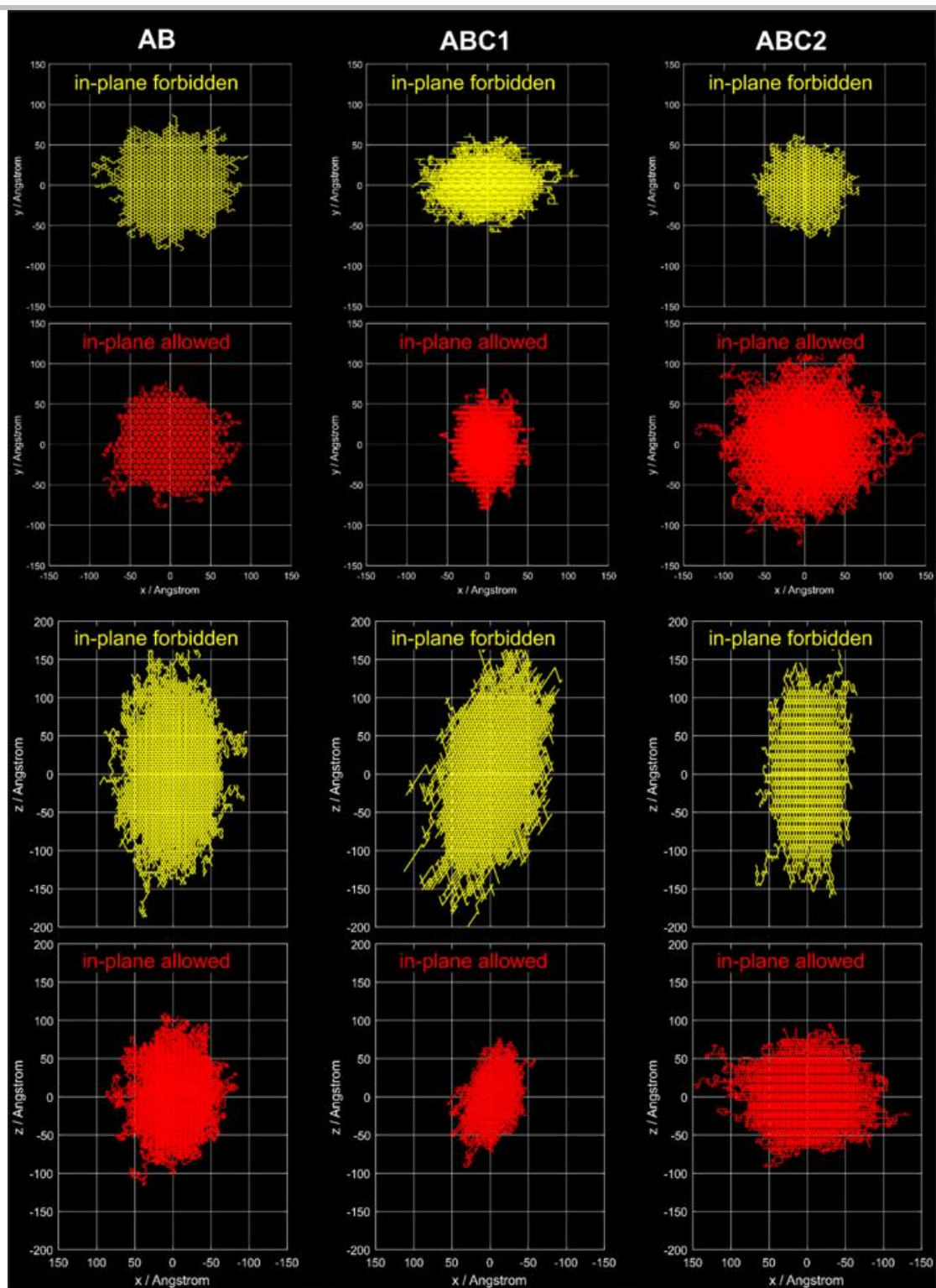


**Figure S13.** Random-walk simulations for a carrier in the three crystal structures under consideration. Yellow trajectories denote in-plane-forbidden transitions, while red trajectories denote in-plane allowed transitions. The upper 6 panels show projections along the z direction; the lower 6 panels depict the same data projected along the y direction.

## References

- [1] G. Algara-Siller, N. Severin, S. Y. Chong, T. Bjorkman, R. G. Palgrave, A. Laybourn, M. Antonietti, Y. Z. Khimyak, A. V. Krasheninnikov, J. P. Rabe, U. Kaiser, A. I. Cooper, A. Thomas, M. J. Bojdys, *Angew. Chem. Int. Ed.* **2014**, *53*, 7450-7455.
- [2] I. Miccoli, F. Edler, H. Pfnur, C. Tegenkamp, *J Phys Condens Matter* **2015**, *27*, 223201.
- [3] M. Tabbal, T. Christidis, S. Isber, P. Merel, M. A. El Khakani, M. Chaker, A. Amassian, L. Martinu, *J. Appl. Phys.* **2005**, *98*.
- [4] aQ. Lv, C. Cao, C. Li, J. Zhang, H. Zhu, X. Kong, X. Duan, *J. Mater. Chem.* **2003**, *13*, 1241-1243; bT. Thomé, J. L. Colaux, P. Louette, G. Terwagne, *J. Electron. Spectrosc. Relat. Phenom.* **2006**, *151*, 19-23; cJ. Jiang, W. Cheng, Y. Zhang, M. Lan, H. Zhu, D. Shen, *Mater. Lett.* **2007**, *61*, 2243-2246; dH. Dai, X. Gao, E. Liu, Y. Yang, W. Hou, L. Kang, J. Fan, X. Hu, *Diamond Relat. Mater.* **2013**, *38*, 109-117.
- [5] C. J. Pickard, A. Salamat, M. J. Bojdys, R. J. Needs, P. F. McMillan, *Phys. Rev. B* **2016**, *94*.
- [6] aT. Ujvári, A. Kolitsch, A. Tóth, M. Mohai, I. Bertóti, *Diamond Relat. Mater.* **2002**, *11*, 1149-1152; bC. Ronning, H. Feldermann, R. Merk, H. Hofsäss, P. Reinke, J. U. Thiele, *Phys. Rev. B* **1998**, *58*, 2207-2215.
- [7] aB. Marinho, M. Ghislandi, E. Tkalya, C. E. Koning, G. de With, *Powder Technology* **2012**, *221*, 351-358; bK. S. Novoselov, A. K. Geim, S. V. Morozov, D. Jiang, M. I. Katsnelson, I. V. Grigorieva, S. V. Dubonos, A. A. Firsov, *Nature* **2005**, *438*, 197-200.
- [8] K. Watanabe, T. Taniguchi, H. Kanda, *Nat. Mater.* **2004**, *3*, 404-409.
- [9] L. Ci, L. Song, C. Jin, D. Jariwala, D. Wu, Y. Li, A. Srivastava, Z. F. Wang, K. Storr, L. Balicas, F. Liu, P. M. Ajayan, *Nat. Mater.* **2010**, *9*, 430-435.
- [10] aA. M. van der Zande, P. Y. Huang, D. A. Chenet, T. C. Berkelbach, Y. You, G. H. Lee, T. F. Heinz, D. R. Reichman, D. A. Muller, J. C. Hone, *Nat. Mater.* **2013**, *12*, 554-561; bO. El Beqqali, I. Zorkani, F. Rogemond, H. Chermette, R. B. Chaabane, M. Gamoudi, G. Guillaud, *Synth. Met.* **1997**, *90*, 165-172.
- [11] H. Yang, S. L. Zhang, L. H. Han, Z. Zhang, Z. Xue, J. Gao, Y. J. Li, C. S. Huang, Y. P. Yi, H. B. Liu, Y. L. Li, *ACS Appl. Mater. Interfaces* **2016**, *8*, 5366-5375.
- [12] X. Qian, Z. Ning, Y. Li, H. Liu, C. Ouyang, Q. Chen, Y. Li, *Dalton Trans.* **2012**, *41*, 730-733.
- [13] aS.-L. Cai, Y.-B. Zhang, A. B. Pun, B. He, J. Yang, F. M. Toma, I. D. Sharp, O. M. Yaghi, J. Fan, S.-R. Zheng, W.-G. Zhang, Y. Liu, *Chem. Sci.* **2014**, *5*, 4693-4700; bH. Ding, Y. Li, H. Hu, Y. Sun, J. Wang, C. Wang, C. Wang, G. Zhang, B. Wang, W. Xu, D. Zhang, *Chem. - Eur. J.* **2014**, *20*, 14614-14618.
- [14] C. Merschjann, S. Tschierlei, T. Tyborski, K. Kailasam, S. Orthmann, D. Hollmann, T. Schedel-Niedrig, A. Thomas, S. Lochbrunner, *Adv. Mater.* **2015**, *27*, 7993-7999.
- [15] D. Schwarz, Y. Noda, J. Klouda, K. Schwarzova-Peckova, J. Tarabek, J. Rybacek, J. Janousek, F. Simon, M. V. Opanasenko, J. Cejka, A. Acharjya, J. Schmidt, S. Selve, V. Reiter-Scherer, N. Severin, J. P. Rabe, P. Ecorchard, J. J. He, M. Polozij, P. Nachtigall, M. J. Bojdys, *Adv. Mater.* **2017**, *29*.
- [16] B. Harbecke, *Appl. Phys. B: Photophys. Laser Chem.* **1986**, *39*, 165-170.
- [17] G. Yin, C. Merschjann, M. Schmid, *J. Appl. Phys.* **2013**, *113*.
- [18] I. H. Malitson, *J. Opt. Soc. Am.* **1965**, *55*, 1205-1209.
- [19] J. Pankove, *Optical Processes in Semiconductors* Dover, New York, **1975**.
- [20] C. Merschjann, T. Tyborski, S. Orthmann, F. Yang, K. Schwarzburg, M. Lublow, M. C. Lux-Steiner, T. Schedel-Niedrig, *Phys. Rev. B* **2013**, *87*.
- [21] J. Metje, M. Borgwardt, A. Mognilevski, A. Kothe, N. Engel, M. Wilke, R. Al-Obaidi, D. Tolkendorf, A. Firsov, M. Brzhezinskaya, A. Erko, I. Y. Kiyani, E. F. Aziz, *Opt. Express* **2014**, *22*, 10747-10760.
- [22] U. Megerle, I. Pugliesi, C. Schrieffer, C. F. Sailer, E. Riedle, *Appl. Phys. B: Lasers Opt.* **2009**, *96*, 215-231.
- [23] S. A. Kovalenko, A. L. Dobryakov, J. Ruthmann, N. P. Ernsting, *Phys. Rev. A* **1999**, *59*, 2369-2384.
- [24] A. A. Raheem, M. Wilke, M. Borgwardt, N. Engel, S. I. Bokarev, G. Grell, S. G. Aziz, O. Kuhn, I. Y. Kiyani, C. Merschjann, E. F. Aziz, *Struct. Dyn.* **2017**, *4*.

## Author Contributions

Y.N. conceived and designed the experiments, performed the synthetic experiments, conducted electrical, AFM, SEM, and FTIR measurements, analyzed the data, and wrote the paper. C.M. conceived the experiments, carried out transient optical spectroscopic and spectrophotometric measurements, executed numerical simulations, analyzed the data, obtained optical parameters, and wrote the paper. J.T. designed and performed electron paramagnetic resonance spectroscopic (EPR) measurements and analyzed the data. P.A. and N.K. carried out x-ray photoelectron spectroscopic measurements and analyzed the data. M.J.B. conceived and designed the experiments, analyzed the data, and wrote the paper.